POLITECNICO DI TORINO
Repository ISTITUZIONALE

Ultrashort pulsed laser texturing of current collector for Si/C Li-ion anodes: Characterization of electrochemical performance and evolution of interface morphology

Original
Ultrashort pulsed laser texturing of current collector for Si/C Li-ion anodes: Characterization of electrochemical performance and evolution of interface morphology / Ravesio, E., Montinaro, G., Mincuzzi, G., Negozio, M., Versaci, D., Gartiser, V., Lutey, A.H.A., Bella, F., Bodoardo, S.. - In: JOURNAL OF ENERGY STORAGE. - ISSN 2352-152X. - 109:(2025). [10.1016/j.est.2024.115226]

Availability:
This version is available at: 11583/2996323 since: 2025-01-07T13:29:31Z

Publisher:
Elsevier

Published
DOI:10.1016/j.est.2024.115226

Terms of use:

This article is made available under terms and conditions as specified in the corresponding bibliographic description in the repository

Publisher copyright

(Article begins on next page)

26 November 2026

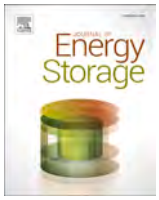
Journal of Energy Storage 109 (2025) 115226



Contents lists available at ScienceDirect

Journal of Energy Storage

journal homepage: www.elsevier.com/locate/est



Research Papers



Ultrashort pulsed laser texturing of current collector for Si/C Li-ion anodes: Characterization of electrochemical performance and evolution of interface morphology

Elisa Ravesio [a], Giorgio Montinaro [a], Girolamo Mincuzzi [b], Marco Negozio [c], Daniele Versaci [a,*], Valentin Gartiser [b], Adrian H.A. Lutey [c], Federico Bella [a], Silvia Bodoardo [a]

[a] Politecnico di Torino, Department of Applied Science and Technology, Electrochemistry Group, Corso Duca Degli Abruzzi, 24, 10129 Turin, Italy
[b] Alphanov, Aquitaine Institute of Optics, Rue F. Mitterrand, 33400 Talence, France
[c] Università degli Studi di Parma, Dipartimento di Ingegneria dei Sistemi e delle Tecnologie Industriali, Parco Area delle Scienze, 181/A, 43124 Parma, Italy

ARTICLE INFO

Keywords:
Laser texturing
Li-ion batteries
Generation 3b
Si/C anodes
Electrochemical performance
Morphology

ABSTRACT

Ultrashort pulsed laser texturing of copper current collectors (CCs) for next-generation Li-ion batteries with composite silicon-graphite anodes is conducted to enhance contact area and improve stress distribution at the interface between CCs and electrode active material. Linearly polarized IR femtosecond laser pulses are used to create sub-micrometric ripples (Cu_L1) and micro-grooves (Cu_L2) via self-modeling phenomena, while direct laser interference patterning (DLIP) with UV femtosecond laser pulses is employed to form micrometric cones (Cu_L3). Pristine (Cu_P) and laser-textured CCs are assembled using half-cell configuration for electrochemical testing, revealing improvements in cyclability and capacity retention with laser-textured CCs. During formation cycles at 0.1C, electrodes with Cu_P CCs exhibit an average specific capacity of 641.8 mAh g^{-1}, whereas those with Cu_L1, Cu_L2, and Cu_L3 CCs achieve 705.3 mAh g^{-1}, 673.0 mAh g^{-1}, and 734.9 mAh g^{-1}, respectively. After 100 cycles, Cu_P electrodes retain 80 % capacity, while laser-textured electrodes show retention of 86.9 %, 83.0 %, and 84.6 %, respectively. AFM analysis of laser-textured CCs before cell assembly indicates a 9–16 % increase in the developed interfacial area ratio (Sdr), with material removal due to laser texturing, <9 %. SEM section analysis before and after electrochemical testing reveals changes in interface morphology, with plastic deformation of CCs due to volumetric changes during charge/discharge cycling. The results suggest that laser texturing helps control plastic deformation at the interface, with SEM analysis providing direct evidence of changes in deformation and stress distribution.

1. Introduction

Lithium-ion batteries (LIBs) have become the electrical energy storage technology of choice for a vast range of products from portable electronic devices to electric vehicles and stationary energy storage due to their excellent combination of energy density, power density and lifespan [1]. Advances in performance, cost, safety and environmental sustainability over the past 30 years have facilitated ongoing uptake, with LIBs currently seen as a critical element for immediate action in mitigating climate change through electrification of the transport industry and implementation of renewable energy systems characterized by intermittent generation such as wind and solar [2,3]. Despite this development, further improvements are required if batteries are to replace fossil fuels across all facets of industry, particularly in transport where energy density and cost continue to be important barriers to update. Next-generation electric vehicles (EVs) must achieve a range of at least 500 km with batteries of reasonable size, weight and cost, requiring increases in energy density and lifespan [4]. Furthermore, the environmental sustainability of the entire product lifecycle is increasingly coming under the spotlight as manufacturers are held accountable for the environmental, health and safety impacts of material extraction, battery manufacturing and end-of-life recycling. These issues require immediate technical solutions to ensure that fossil fuel energy sources can be phased out in view of achieving global net zero emissions by 2050.

Improving the performance of LIBs requires the development of new

* Corresponding author.
E-mail address: daniele.versaci@polito.it (D. Versaci).

https://doi.org/10.1016/j.est.2024.115226
Received 11 October 2024; Received in revised form 12 December 2024; Accepted 26 December 2024
Available online 30 December 2024
2352-152X/© 2024 The Authors. Published by Elsevier Ltd. This is an open access article under the CC BY-NC-ND license (http://creativecommons.org/licenses/by-nc-nd/4.0/).

active materials with higher energy density and greater stability [5,6], while at the same time ensuring that the binder, conductive additive and current collector are optimized for a given composition [7]. Next-generation active materials such as silicon-graphite anodes undergo large volumetric changes during charge and discharge cycling, placing greater importance on the binder and current collector to ensure sufficient mechanical strength to avoid cracking or delamination, which lead to rapid cell breakdown and limited lifespan [8]. Within LIB electrodes, the current collector (CC) plays a fundamental role in guaranteeing unimpeded migration of electrons to and from the active material, as well as structural support during cell production and assembly processes such a calendering, winding and z-folding [4,9]. Pure copper and aluminum films with thicknesses in the range 4–6 μm [10] are currently employed for anode and cathode CCs in commercial LIBs due to their electrochemical stability under normal operating conditions [11]. Further to limiting maximum mechanical stresses in the CC and active material, complete contact and sufficient adhesion must be achieved at the interface between the CC and active material throughout the entire lifespan of the cell [12]. These aspects are interrelated, as the current collector acts as a local constraint to expansion and contraction of the active material during lithiation and de-lithiation, thus influencing stresses within both materials at and near the interface. The properties and topography of CCs are therefore of fundamental influence on LIB electrode performance [5,13–15].

Chemical etching and structuring of CCs to increase the roughness and wettability prior to deposition of the active material, together with application of carbonaceous coatings to inhibit corrosion phenomena, are well-established techniques for modifying surface properties to improve battery performance in terms of coulombic efficiency, capacity retention and specific capacity [12,13,16–21]. Delamination and cracking at the interface between the CC and active material are nonetheless ongoing issues for next-generation active materials undergoing large volumetric changes during charge and discharge cycling. Loss of mechanical integrity leads to rapid capacity fade due to an increase in electronic resistance and consequent reduction in mobility of lithium ions [15]. Further to being expensive, chemical etching also presents non-trivial environmental and safety issues, which are becoming increasing problematic for manufacturers as they seek to improve the eco-sustainability of their supply chains. Pulsed laser texturing has recently emerged as a sustainable alternative for increasing the surface roughness of CCs and improving mechanical adhesion between the CC and active material.

Laser materials processing has a consolidated role in LIB manufacturing for a range of processes from cutting of electrodes and separator films, to welding of current collector tabs and battery-pack bus bars [22,23]. Laser texturing of complete electrodes has been explored as a way of modifying ionic diffusion to enable fast charging via dual-pore networks [24,25]. Laser texturing of CCs instead requires precise control of process parameters to increase the effective surface area as much as possible while limiting the depth and quantity of removed material to ensure that structural integrity is not compromised. Nanosecond pulsed laser texturing has been shown to increase mechanical adhesion between aluminum and copper CCs and $LiFePO_4$ (LFP) active materials [26], leading to improved cyclability of cathode half cells [27]. While being characterized by considerably lower cost than shorter laser pulses, this approach has important limitations in terms of the aspect ratio of surface features that can be achieved via ablation, as well as distortion induced by both material removal and thermal loading during nanosecond pulsed laser exposure. Ultrashort pulsed laser texturing instead leads to far more limited thermal loading on the target material while introducing the possibility of exploiting a variety of surface texturing techniques such as direct laser interference patterning (DLIP) [28], submicrometric laser-induced periodic surface structures (LIPSS), micro-grooves (μ-grooves) and micro-spikes generated by self-remodeling phenomena [29,30], and complex hierarchical structures achieving increases in effective surface area with minimal or no material ejection or substrate deformation [31]. While the investment cost required for implementation of an ultrashort pulsed laser system represents a legitimate barrier to uptake, this aspect is offset by the relatively low energy density required to produce LIPSS compared to nanosecond pulsed laser ablation and potential gains in terms of product value resulting from increased energy density and/or lifespan of the battery. Hierarchical micro/nanostructures obtained with femtosecond or picosecond laser pulses on aluminum and copper CCs have been shown to improve the capacity retention of $LiNi_{0.5}Co_{0.2}Mn_{0.3}O_2$ (NCM) [32] cathodes compared to untextured CCs while allowing graphite anodes to maintain high capacity beyond 600 cycles [33].

The true value of femtosecond laser texturing in this field, however, lies in the ability to improve the capacity retention of next-generation high energy density active materials that are currently limited by mechanical failure of the active material or delamination at the interface between the CC and active material. Of particular interest are next-generation composite silicon-graphite anodes that undergo very large volumetric expansion during lithiation; approximately 28 % expansion with 10 % silicon. The present work therefore investigates the electrochemical performance of composite silicon-graphite anode half cells with femtosecond laser-textured copper CCs. Three different strategies are employed to achieve submicrometric LIPSS, μ-grooves and micrometric cones, with the electrochemical performance of anode half-cells with and without textured CCs compared. Further to demonstrating tangible improvements in cell performance with laser texturing, mechanical characterization of electrodes prior to assembly and in-depth post-cycling analyses provide insight into the mechanisms leading to such improvements. The outcomes suggest that investment into ultrashort pulsed laser texturing is warranted in pursuit of improved LIB performance, higher product value, and ultimately greater sustainability.

2. Materials and methods

2.1. Laser texturing of copper current collector

Two batches of copper CCs were textured with distinct techniques employing femtosecond laser pulses. In the first, CCs were textured by exploiting self-modeling phenomena. To achieve this, a Gaussian ($M^2 = 1.1$), linearly polarized IR femtosecond laser (Amplitude Tangerine HP) with a wavelength of $\lambda = 1030$ nm, pulse duration of $\tau = 330$ fs, maximum repetition rate of $f = 2$ MHz and maximum average power of $P = 34$ W was employed, together with a galvanometric scanner (Scanlab Excelliscan 14) and f-theta focusing lens with focal length of $f = 100$ mm, achieving a beam focus with diameter $d_0 \approx 60$ μm ($1/e^2$ of the intensity profile). Texturing was performed over 20 mm × 20 mm areas of copper CCs with a fixed repetition rate of $f = 1$ MHz, scanning speed of $v = 2.5\ m{\cdot}s^{-1}$ and hatch distance of $h = 10$ μm, achieving a nominal pulse overlap of 96 % in the scanning direction and 83 % in the lateral direction. The number of scans was varied between $N = 1$ and $N = 20$ and the pulse energy between $E = 0.85$ μJ and $E = 30$ μJ. The resulting energy dose, as defined in Eq. (1) [30,34], was therefore between $\Phi = 13.6\ mJ{\cdot}cm^{-2}$ and $9.6\ J{\cdot}cm^{-2}$.

$$\Phi = N\frac{E{\cdot}f}{h{\cdot}v} \tag{1}$$

In the second batch of CCs, texturing was accomplished via DLIP using the same laser source and converting the beam from IR to UV via third harmonic generation to achieve a wavelength of $\lambda = 343$ nm. The beam was then split into two identic sub-beams, which were made parallel by a prism. The two beams were then fed into the same galvanometric scanner as in the previous case (but with UV coatings), then focused and superposed by an f-theta lens with a focal length of $f = 60$ mm. The resulting 1D interference pattern was characterized by a fringe period of $\Lambda = 2.8$ μm, as measured by a CCD camera with a pixel size of 1.6 μm (IDS μEye). In this case, texturing was performed over 10 mm ×

10 mm with a fixed repetition rate of f = 100 kHz and scanning speed of v = 0.4 m s^{-1} in the fringe direction, performing a single pass ($N = 1$) with a hatch distance h = 11 μm. As a result, a regular 1D pattern was written onto the copper surface. Texturing was then repeated after rotating the sample by 90° to obtain a regular 2D pattern. During tests, the aspect ratio of surface structures was maximized by varying the pulse energy between E = 0.38 μJ and E = 13.4 μJ.

From the two batches we identified 3 different, most promising set of parameters (see Table 1) which were used to extend the texturing over CCs as large as 11 cm × 8 cm. The last were used for the fabrication of complete anodes.

2.2. Morphology and topography characterization of laser-textured CCs

Scanning electron microscopy (SEM, TESCAN VEGA3) was performed on all laser-textured CCs with an acceleration voltage of 10 kV. Preliminary acquisition of the surface topography was performed during the preparation of laser-textured CCs with a confocal microscope (Zeiss SmartProof 5). Detailed acquisition of the surface topography of CCs employed for electrochemical tests was then performed with an atomic force microscope (AFM, Veeco Dimension 3100 SPM) equipped with a silicon cantilever with 8 nm conical radius of curvature. The instrument was operated in tapping mode, with 256-line acquisitions performed over representative 50 μm × 50 μm and 20 μm × 20 μm regions of all laser-textured samples. Topography data was exported as a cloud of points to allow calculation of the developed interfacial area ratio (Sdr) in line with ISO 25178. This parameter, defined as the ratio of the actual surface area to the projected surface area, represents the percentage increase in surface area compared to a perfectly flat surface. Values of Sdr were measured as <1.5 % for untextured copper CCs, implying proximity to a perfectly flat surface. Values of Sdr for laser-textured surfaces were therefore interpreted as representing the percentage increase in surface area compared to untextured CCs. The volume change, consequent to the laser texturing (∇V), was approximated by considering a horizontal plane in contact with the highest point of each surface and calculating the volume between the plane and the acquired surface over the entire acquisition area. This method led to an overestimation of the volume due to surface irregularities and local peaks but was nonetheless useful in providing an upper bound for the quantity of material removed during laser processing.

2.3. Contact angle measurements

Water contact angle measurements were performed on pristine and laser-textured CCs (Kruss DSA 100 DropShape Analyzer) to quantify changes in wettability induced by the various laser treatments and provide qualitative insight into compatibility of water-based slurries with the CC surfaces. A lower contact angle indicates higher surface affinity, implying an easier and more effective coating process, leading to better adhesion. All tests were performed following the same protocol, with 20 mm × 20 mm laser textured areas used directly without any additional pre-treatment or cleaning so as to represent realistic surface conditions in a high throughput industrial production environment. Milli-Q water was used as the liquid for all tests, with the contact angle measured every 30 s for 3 min, resulting in a total of six measurements per sample. Average values and an approximation of error were obtained in each case.

Table 1
Summary of laser texturing.

Sample name	*Type of structures*	*Texturing technique*	*Main laser parameter*
Cu_L1	LIPSS	Self-remodeling	Φ = 96 mJ·cm^{-2}
Cu_L2	LIPSS and μ-grooves	Self-remodeling	Φ = 280 mJ·cm^{-2}
Cu_L3	Cones	DLIP	E = 1.3 μJ
Cu_P	Pristine	Untextured	–

2.4. Anode preparation and electrochemical characterization

The active material used in this work was provided by Nanomakers. Detailed information and characterization of the Si/C material are available in the work by Gutierrez et al. [35]. The active material is a composite of pitch-derived carbon and graphite-based Si/C/Gr, with a silicon content of 12 wt%. More specifically, silicon nanoparticles and graphite particles are embedded in an amorphous matrix formed through pitch pyrolysis. According to Gutierrez et al. [35], the silicon is crystalline, with all silicon particles coated with an approximately 2 nm thick amorphous carbon layer produced via laser pyrolysis. All relevant information regarding the active material used in the present work is summarized in Table S1.

The active material was mixed with Carbon Black C-NERGY C65 (Imerys Graphite & Carbon Corporation) conductive additive (CA) and sodium carboxy methyl cellulose Na-CMC (DAICEL 2200) as the main binder, together with styrene butadiene rubber (SBR Arlanxeo) additive to improve the mechanical properties of the final electrode. The materials were mixed with milliQ water using a disperser (Dispermat) to achieve a constant solid fraction of 33 % and solid component proportions of 90:2:4:4 wt% AM, CA, binder and additive. To achieve this, Na-CMC was firstly weighted and transferred into a 25 mL beaker with 9.70 mL of milliQ water and stirred at 1000 RPM for 1 h to guarantee complete dissolution of the binder inside the solvent. The CA was then added and the slurry stirred for an additional 30 min at 2200 RPM. After this, the AM was added and the slurry mixed at the same speed for an additional hour. Finally, the SBR was added and the mixing speed lowered to 400 RPM to avoid degradation of the SBR chains. The wet slurry was then cast onto pristine and laser-textured CCs via the Doctor Blade technique using an automatic film applicator (Sheen 1133 N) at a speed of 10 mm s^{-1} to achieve a deposition thickness of 100 μm. Wet electrode sheets were dried in ambient air for 2 h and subsequently in an oven for 16 h at 80 °C. Discs of area 1.539 cm^2 and 0.785 cm^2 were then punched from the complete electrodes with an MSK-T-07 compact precision disc cutter and vacuum dried at 80 °C (Büchi B-585 glass oven) for 24 h before cell assembly. The final active material loading was in the range between 2.5 mg cm^{-2} and 3.5 mg cm^{-2} for all samples.

The total resistance and the interfacial resistance between the active layer and current collector of the obtained electrode were measured using a 46-point probe system (RM2610, HIOKI Corp., Japan) at room temperature. During the analysis, constant current was applied, creating a three-dimensional current distribution within the electrode film while voltage probes detected the potential distribution across the film. The potential distribution was analyzed using numerical methods based on the finite volume method to determine the electrode resistance and interfacial resistance. This methodology permitted independent evaluation and quantification of electrode and interfacial resistance contributions between the active layer and current collector.

The cell assembly process was carried out inside an Ar-filled glove box (MBraun Labstar, H_2O and O_2 content <1 ppm). The 1.539 cm^2 electrodes were assembled into 2032 coin cells with Li disks as counter electrodes (Ø15.6 mm, thickness 0.56 mm, MTI Corp). Glass Fiber (Whatman GF/D, thickness 0.65 mm) was used as a separator and soaked with 150 μL electrolyte solution comprising 1 M $LiPF_6$ mixed with a 1:1 v:v solution of ethylene carbonate (EC) and diethylene carbonate (DEC), with 10 wt% fluoroethylene carbonate (FEC) and 2 wt% vinyl carbonate (VC).

The prepared cells were subject to galvanostatic charge-discharge cycling (CG) with an Arbin LBT-21084 at different current regimes within the voltage range of 0.01–1.5 V. Cells first underwent lithiation from OCV up to 0.01 V at constant applied current of 0.1C, after which a constant voltage step of 0.01 V was applied up to 0.01C, finally cells were de-lithiated up to 1.5 V at constant applied current of 0.1C. This forming process was repeated three times. The rate capability test was then performed at different C-rates (0.2C, 0.5C, 1C, 2C) and, after each lithiation step, a constant voltage step was applied up to 0.02C. Finally,

cells were cycled at 1C for 80 cycles with the same CCCV protocol to evaluate capacity retention. The complete cycling protocol is reported in Table S2. For each sample, electrochemical tests were replicated and averaged over a minimum of three cells.

A three-electrode configuration was used for cycling voltammetry analysis. The 0.785 cm^2 electrodes were assembled with Li disks as both counter electrode and reference. Cycling voltammetry analysis was performed within the voltage range 0.1–1.5 V with a scanning rate of 0.1 V s^{-1} on a versatile multichannel potentiostat (VMP-3 Biologic). All electrochemical performance tests were undertaken at room temperature.

Electrochemical characterization of the current collectors was performed using cyclic voltammetry (CV) to detect any potentially undesirable/parasitic redox reactions resulting from laser texturing. Tests were conducted in a standard three-electrode setup (T-cell), where two 10 mm diameter disks cut from each type of collector were paired with a lithium reference electrode. Separators used for tests were of the same diameter and made of glass fiber (Whatman). 140 µL of electrolyte (1 M $LiPF_6$ in DEC 1:1 (wt.) + 10 wt% FEC + 2 wt% VC) was used, with tests conducted within a potential range of 0.1–1.5 V at a scanning rate of 0.1 mV s^{-1} using a laboratory potentiostat (Biologic VMP-3).

Potentiostatic electrochemical impedance spectroscopy (PEIS) analyses were conducted on a versatile multichannel potentiostat (VMP-3 Biologic). Alternative Current (AC) impedance measurements were performed before cycling with an amplitude of 10 mV over a frequency range of 100 kHz–100 MHz.

2.5. Post-cycling electrode characterization

The morphology of sectioned electrodes before and after cycling was analyzed with a SEM (dual beam FESEM/FIB Zeiss Auriga Compact) equipped with a secondary electron (SE) detector. Electrodes were firstly prepared by mechanically cutting 10 mm × 10 mm pieces from the center of complete electrodes, which were then cold mounted in conductive resin (Tecmet2000, TEC-BLACK). Samples were placed in a vertical position with the section of interest, normal to CC surface features, held facing downwards. Grinding was performed with P80 grit abrasive paper to a depth of at least 1 mm to ensure that any modification caused by cutting the electrodes was removed. The surface was then mechanically ground with abrasive paper ranging from P240 to P4000 grit, followed by polishing with a water-free diamond suspension and lubricant immediately prior to SEM analysis.

3. Results and discussion

As mentioned in the experimental section, two batches of copper CCs were textured with distinct techniques employing femtosecond laser pulses. For the first batch, self-modeling phenomena were exploited to achieve various surface topographies at different levels of applied energy dose Φ, as depicted in SEM micrographs shown in Fig. 1(a)-(d). As discussed in the literature, Φ represents a key parameter driving the evolution of surface structures from LIPSS to µ-grooves and then microspikes [36]. For relatively low values of energy dose (Φ = 72 mJ·cm^{-2}, E = 2 µJ, N = 3), LIPSS perpendicular to the polarization direction was observed within some regions but not others,(Fig. 1(a)). This effect was likely the result of local surface inhomogeneity leading to minor variations in optical reflectivity, preventing homogeneous generation and propagation of surface polaritons, leading to inhomogeneous texturing [37]. By increasing the energy dose (Φ = 96 mJ·cm^{-2}, E = 6 µJ, N = 1), a homogeneous distribution of LIPSS was observed (Fig. 1 (b)). A ripple period of Λ ≈ 850 nm was extracted, which was in line with values reported in the literature [38]. By increasing the energy dose further (Φ =

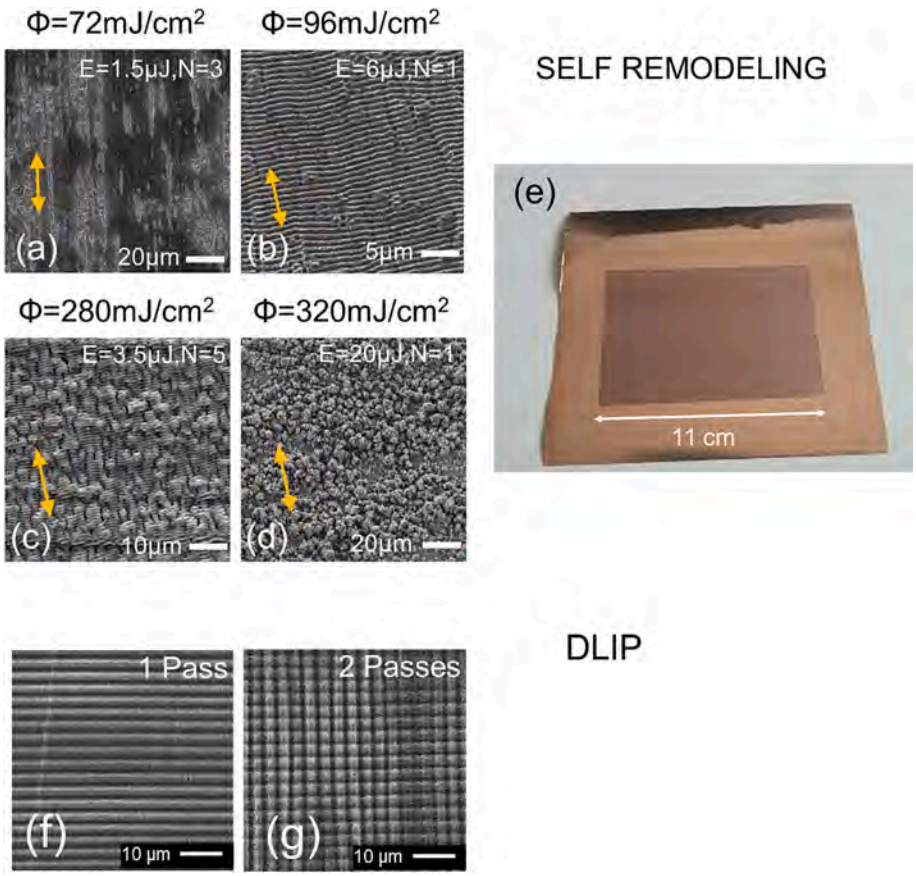


Fig. 1. SEM micrographs of laser textured CCs from the first batch (self-remodeling) (a)-(d), photograph of textured CC with µ-grooves (e), SEM micrographs of laser textured CCs from the second batch (DLIP) (f)-(g).

280 μJ·cm^{-2}, E = 3.5 μJ, N = 5), μ-grooves parallel to the polarization direction were generated on CC surfaces together with LIPSS (Fig. 1 (c)). As a consequence, a 2D pattern was obtained, enhancing the surface-to-area ratio (see Fig. 2). The greater number of laser scans in this case, however, led to processing times that were five times higher than for 1D LIPSS. Finally, by increasing the energy dose further again (Φ = 320 μJ·cm^{-2}, E = 20 μJ, N = 1), micrometric spikes were generated (Fig. 1 (d)) in line with the literature [37]. In contrast to the previous case, mechanical deformation of CCs was observed, rendering this parameter set unsuitable for electrode fabrication. Based on these outcomes, LIPSS (Cu_L1) and μ-grooves (Cu_L2) were produced over larger surfaces for electrode preparation. Fig. 1(e) displays a photograph of a textured CC with μ-grooves over an area of 120 mm × 100 mm, where macroscopic deformation was not observed.

Analogously, SEM micrographs of laser-textured CCs from the second batch of experiments are shown in Fig. 1(f)-(g), where DLIP was employed to achieve surface modification. The surface-to-area ratio of structures obtained after texturing was optimized by increasing the aspect ratio as much as possible while avoiding mechanical deformation of the CCs. As DLIP is based on material ablation, it was possible to increase the aspect ratio by increasing the pulse energy E. Fig. 1(f) shows the best case obtained with E = 1.3 μJ after a single pass. Higher values of laser pulse energy were instead found to induce mechanical deformation. The sample was then rotated by 90° and textured a second time using the same set of parameters to achieve cone structures (Fig. 1(g)).

Subsequently, the surface topography of all laser-textured CCs used for cell preparation (Cu_L1, Cu_L2, Cu_L3) was acquired via AFM to calculate the developed interfacial area ratio, as presented in Fig. 2. Measurements performed over areas of 50 μm × 50 μm show the presence of fine structures deriving from laser texturing superimposed on larger-scale ridges and valleys resulting from the underlying surface morphology of the CCs prior to texturing. While features deriving from the original surface and laser texturing were similar in vertical magnitude, it is important to note that the developed interfacial area ratio (Sdr) strongly depends on the aspect ratio and therefore in-plane density of surface features. While still exhibiting some irregularity due to the underlying morphology of the CCs, measurements performed over areas of 20 μm × 20 μm better isolated fine structures resulting from laser texturing. LIPSS (Cu_L1) could be observed as parallel ridges with a period of approximately 850 nm and a height of approximately 300–500 nm. μ-grooves (Cu_L2) instead exhibited a more complex hierarchical topography with LIPSS superimposed on larger structures with a period of approximately 3–4 μm and height of approximately 0.8–1.2 μm. DLIP instead led to a series of square cones (Cu_L3) with base dimensions of approximately 2.8 μm × 2.8 μm and heights of approximately 0.8–1.2 μm.

Values of Sdr, considered representative of the increase in surface area compared to pristine CCs, were 9 % for Cu_L1, 16 % for Cu_L2 and 9 % for CU_L3. The value of Sdr for a given surface depends primarily on the aspect ratio of surface features, which were similar for Cu_L1 and CU_L3, leading to similar values of Sdr. More complex hierarchical structures achieved on Cu_L2 led to a greater increase in effective surface area. The calculated volume of removed material ($-\nabla V$) was 5.0 % for Cu_L1, 6.0 % for Cu_L2 and 8.6 % for Cu_L3. As noted previously, this value was considered an upper bound due to the method used for its calculation, suggesting that all laser texturing strategies limited material removal to below 9 %. In particular, LIPSS are generally considered to lead to negligible material removal, suggesting that the calculated value of ∇V for Cu_L1 was simply due to changes in surface topography. DLIP, on the other hand, leads to material removal via ablation for which a finite volume of material removal was expected for Cu_L3. Values were nonetheless low, suggesting limited impact on the mechanical properties of copper CCs. This outcome was confirmed by the lack of thermally or mechanically induced deformation of CCs following laser texturing.

To assess the impact of collector surface texturing on the electrode manufacturing process, contact angle measurements were conducted on the three laser-treated CCs and the pristine ones. Water contact angle images are presented in Fig. 3, where it can be observed that all surfaces

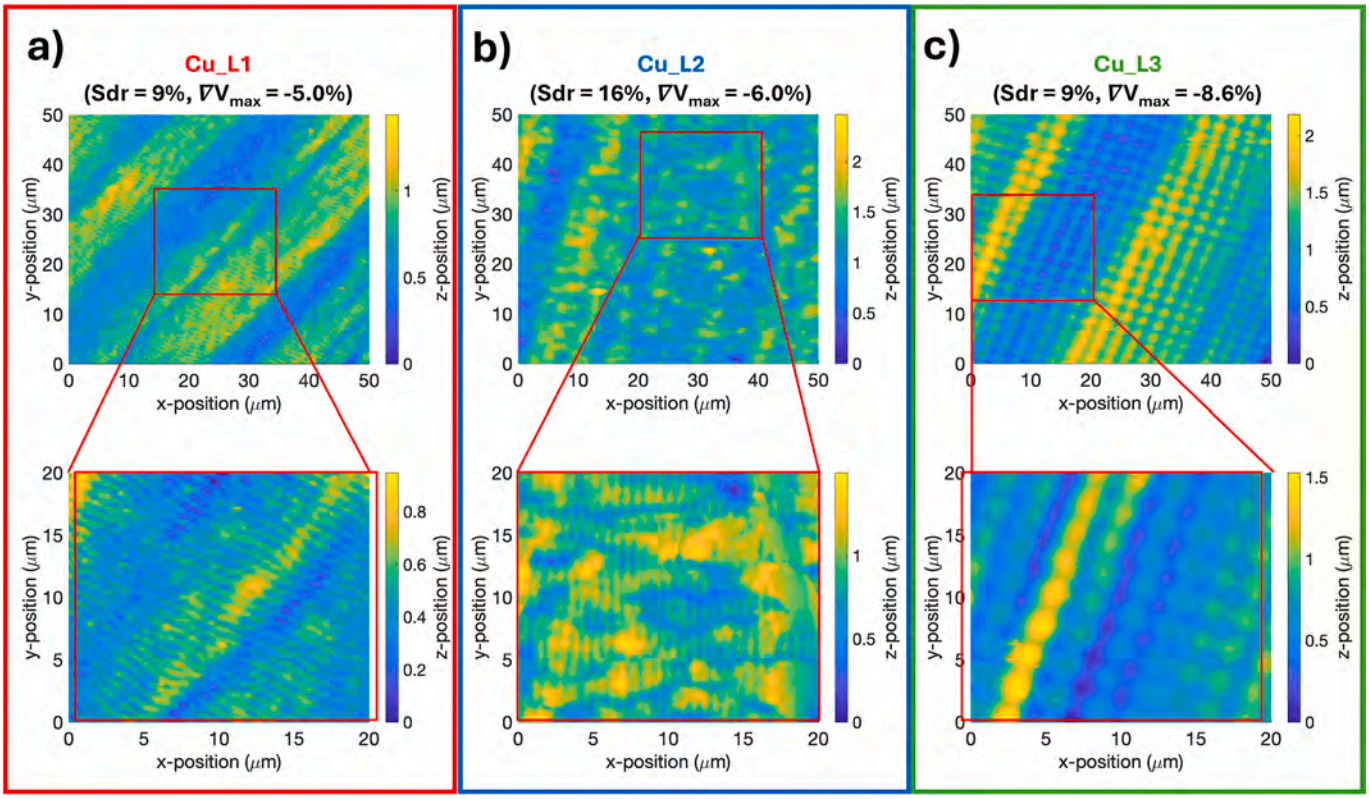


Fig. 2. Topography of laser-textured CCs acquired via AFM: Cu_L1 (a), Cu_L2 (b), Cu_L3 (c).

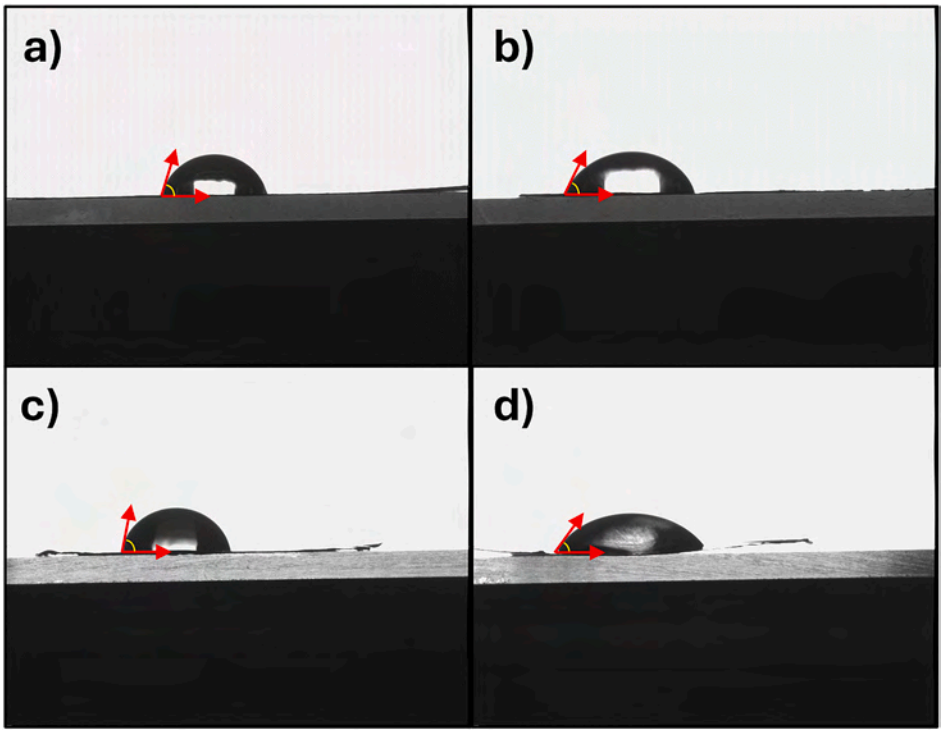


Fig. 3. Contact angle images of Milli-Q water droplets on Cu_P (a), Cu_L1 (b), Cu_L2 (c), Cu_L3 (d).

exhibited mild hydrophilicity but with no significant spreading of droplets. Table 2 presents the measured contact angle in each case. Laser texturing with DLIP (Cu_L3) yielded highest wettability (lowest contact angle), while the other laser-textured surfaces (Cu_L1 and Cu_L2) exhibited slight increases in contact angle compared to pristine samples, implying lower wettability. These observations suggest that a slurry applied to Cu_L3 CCs would more easily spread and possibly achieve better adhesion, leading to better electrochemical performance and thus more efficient cells [39–41].

Subsequently, all the CCs were analyzed by cyclic voltammetry (0.1 mV s^{-1} range of 0.1–1.5 V), using lithium metal as counter and reference electrodes and 1 M $LiPF_6$ in DEC 1:1 (wt.) + 10 wt% FEC + 2 wt% VC as electrolyte, to evaluate the electrochemical stability of the laser-treated current collectors under cell operating conditions. Analysis of cyclic voltammetry curves obtained with laser-textured CCs (Fig. S1) exhibited no notable secondary/undesirable reactions. Despite the noise from the measurement setup, profiles for each type of collector were consistent and stable within the considered potential range, typical of common anodic materials, and comparable across successive cycles. The absence of peaks indicates the absence of reactive species that could affect the cycling performance of anodic materials coated on the tested CCs, effectively making them viable candidates for electrochemical use and comparison with pristine copper CCs.

After establishing the electrochemical stability of the laser-textured collectors, silicon-based anode electrodes were fabricated and analyzed. The internal resistance of a cell typically manifests as an IR drop during charge/discharge processes, significantly affecting the specific capacity and energy efficiency of the cell [42]. In particular, the electronic and ionic conductivity of the electrode plays a significant role in determining the internal resistance of the cell. Consequently, the electronic conductivity of the electrode is a critical factor influencing its electrochemical performance. Within this context, modifications to the current collector can have a non-trivial impact on the electrical conductivity of the entire electrode. Therefore, the electrode resistance and interfacial resistance between the active layer and current collector were measured using a 46-point probe system at room temperature [43–45]. The results of this analysis are presented in Table 3.

From the obtained results it can be observed that the current collectors treated with LIPSS exhibit slightly higher resistivity values, considering both the composite volume resistivity and the interface resistance. In this context, it is important to note that, when considering only the composite volume resistivity, this value should theoretically remain almost unchanged since the materials involved are the same. Focusing on the interface resistance, this parameter appears more relevant, further confirming that the DLIP laser treatment reduces the resistance compared to the other two laser treatments. The lower resistance observed for Cu_3L can be attributed to its more uniform pattern compared to Cu_1L and Cu_2L. A lower interfacial resistance between the current collector and active layer positively impacts the electrochemical performance of the electrode by enhancing electronic conductivity.

Consequently, the prepared silicon-based electrodes with different CCs were first subjected to cycling voltammetry, allowing comparison between those with pristine and laser-textured CCs. This analysis was performed within the voltage range of 0.1–1.5 V with a scanning rate of

Table 2
Measured values of water contact angle on different types of CC.

Sample name	Contact angle (MilliQ water)
Cu_P	73.4° ± 0.7°
Cu_1L	64.4° ± 0.6°
Cu_2L	78.6° ± 0.5°
Cu_3L	53.7° ± 0.7°

Table 3
composite volume resistivity and interface resistance of electrodes with different laser-treated current collector.

Sample	*Composite resistivity (Ω cm)*	*Interface resistance (Ω cm^2)*
Cu_P	1.89×10^{-1}	8.64×10^{-4}
Cu_1L	2.85×10^{-1}	4.16×10^{-3}
Cu_2L	2.45×10^{-1}	3.37×10^{-3}
Cu_3L	1.63×10^{-1}	5.30×10^{-4}

0.1 mV s^{-1}, as shown in Fig. 4. All curves were normalized to the weight of the active material. The comparison of the first cycle of each cyclic voltammogram (Fig. 4(a)) confirmed lithiation of silicon and structural changes due to the formation of Li—Si alloy (from crystalline to amorphous phase). In general, similar behavior was observed for all the samples; however, some differences in peak intensity were noted. In relation to the lithiation process, a broad cathodic peak was evident at around 0.75 V due to solid electrolyte interphase (SEI) formation on particle surfaces for all samples (Cu_P, Cu_L1, Cu_L2, Cu_L3) [46]. This indicates that SEI layer formation was not affected by the laser treatment for this specific lithiation step. At lower voltages, a characteristic cathodic peak at around 0.2 V was observed, which typically corresponds to the lithiation of silicon, forming a metastable Li—Si amorphous (Li_xSi) phases [47–50]. The peak exhibited different intensities and shifts depending on the sample. Specifically, Cu_P showed a broad and less defined peak around 0.18 V, while Cu_L2 exhibited a similar profile with a peak potential around 0.20 V. Conversely, Cu_L1 and Cu_L3 showed more defined peaks at 0.17 V and 0.22 V, respectively. Notably, the electrode with CC textured via DLIP (Cu_L3) exhibited a more intense and defined peak, shifted to higher potentials, highlighting lower polarization of the cell. This lower polarization means more efficient utilization of the active material, which is reflected by a higher current intensity value and more pronounced peak. This observation aligns with the lower resistivity observed for the Cu_L3 current collector, supporting the idea that the Cu_L3 surface structure ensures better adhesion of the active material, leading to enhanced utilization of the active material during the electrochemical reaction.

A second prominent cathode peak was visible at lower potentials, close to the cut-off potential of 0.1 V, due to the phase transition from amorphous Li_xSi to crystalline $Li_{15}Si_4$ [47]. The shift in this peak was less prominent and consequently more defined and intense for Cu_L3. It is important to note that lithiation of graphite or amorphous carbon also occurred during the first cycle, superimposed on lithiation of the silicon [51,52].

During the anodic scan, two main oxidation peaks were observed around 0.19 and 0.2 V. The first peak was characteristic of de-lithiation of graphite and amorphous carbon, while the second peak was attributed to dealloying of silicon [52,53]. A third broad peak was partially visible at higher potentials (0.49 V), which was attributed to a further silicon dealloying step [54]. Different behaviors were again identified depending on the CC employed. Cu_P and Cu_L1 exhibited a defined peak at 0.25 V and a less-defined one at lower voltage. In contrast, Cu_L2 and Cu_L3 presented two well-defined peaks at 0.20 V and 0.26 V. Similar to the cathodic branch, the anodic branch peak intensities could be associated with a lower overpotential and improved electronic conductivity, which was particularly noteworthy for Cu_L2 and Cu_L3 [12].

Fig. 4(b) compares the third cycle of cyclic voltammetry tests. Both the cathodic and anodic peaks were located at approximately the same voltage observed during the first cycle. The current intensities of both cathodic and anodic peaks increased with the number of cycles due to the activation process of the electrode active material, as previously observed in other studies [55] As reported by Jiang et al., this effect can be associated with the development of the amorphous Li—Si phase, which depends on the transport rate of lithium ions into the bulk silicon and causes gradual breakdown of the crystalline silicon structure [56].

More generally, the different CC treatments appeared to impact the intensity of cathodic peaks at lower voltages. This effect could be attributed to the roughness of the CC surface, which may have reduced the charge transfer resistance [12]. In particular, uniform and homogeneous texturing of the Cu_L3 collector ensures improved contact between the current collector and active material, facilitating electronic exchange between the materials.

To better clarify the role of laser-treated CCs, AC impedance measurements were performed on assembled half-cells before cycling. All Nyquist plots were fitted using the equivalent circuit reported in Fig. S3, with the fitted results reported in Table S3, where Rel represents the resistance of the electrolyte solution and Rct the charge-transfer resistance at the electrode/electrolyte interface. While the Rel is similar for all electrodes, the most significant differences can be observed in the Rct. Specifically, higher resistance values are noted for cells with Cu_P and Cu_L2 collectors, whereas electrodes with Cu_L1 and, in particular, Cu_L3 exhibit lower resistance. These results corroborate the observation obtained from cyclic voltammetry analysis, where the Cu_L3 electrode demonstrated lower polarization, which is directly associated with lower internal resistance.

Following the results obtained from cyclic voltammetry, all electrodes were subjected to repeated charge and discharge cycles at varying C-rates. The cycling performance of electrodes with the different CCs is presented in Fig. 5. During the three initial forming cycles at 0.1C, all electrodes with laser-treated collectors exhibited higher specific capacity compared to those with the pristine current collector (Fig. 5(a, b)). In particular, during the first forming cycle at 0.1C, cells with Cu_P electrodes exhibited an average specific capacity of 641.8 mAh g^{-1}, while those with laser textured CCs achieved 705.3 mAh g^{-1}, 673.0 mAh g^{-1} and 734.9 mAh g^{-1} for Cu_L1, Cu_L2 and Cu_L3, respectively (Fig. 5(a)). This indicates that the specific capacity was greater with laser-textured current collectors from the first cycles.

A similar trend was observed at higher C-rates (Fig. 5(a)), with visible differences observed at 2C, where Cu_P exhibited an average specific capacity of 605.8 mAh g^{-1}, significantly lower than the values obtained for cells with laser-textured CCs. At 2C, comparable values were observed for Cu_L1 and Cu_L2 (~ 650 mAh g^{-1}) while Cu_L3 exhibited average capacity values of approximately 695 mAh g^{-1}. Comparing the entire rate capability process (Fig. 5(b)), it can be observed that the specific capacity values remained higher for Cu_L3.

In relation to the Initial Coulombic Efficiency (I.C.E.), this value was

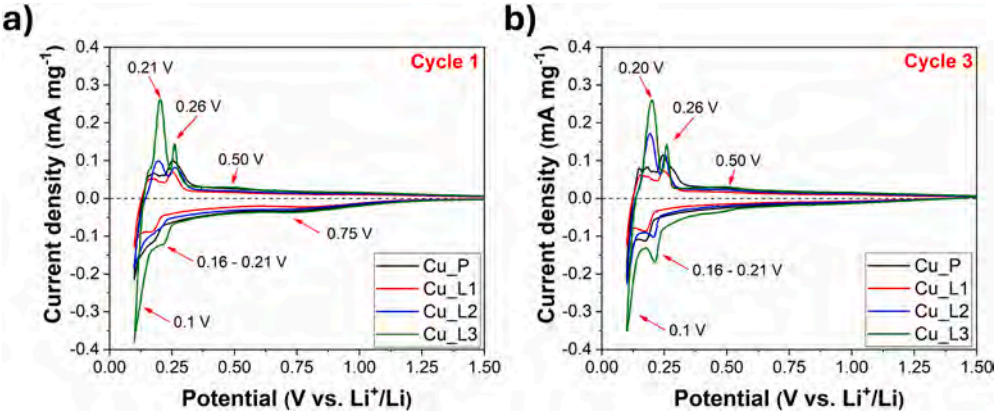


Fig. 4. Cyclic voltammetry comparison of Si/C electrodes obtained using different copper CCs: first cycle (a) and third cycle with a scanning rate of 0.1 mV s^{-1} (b).

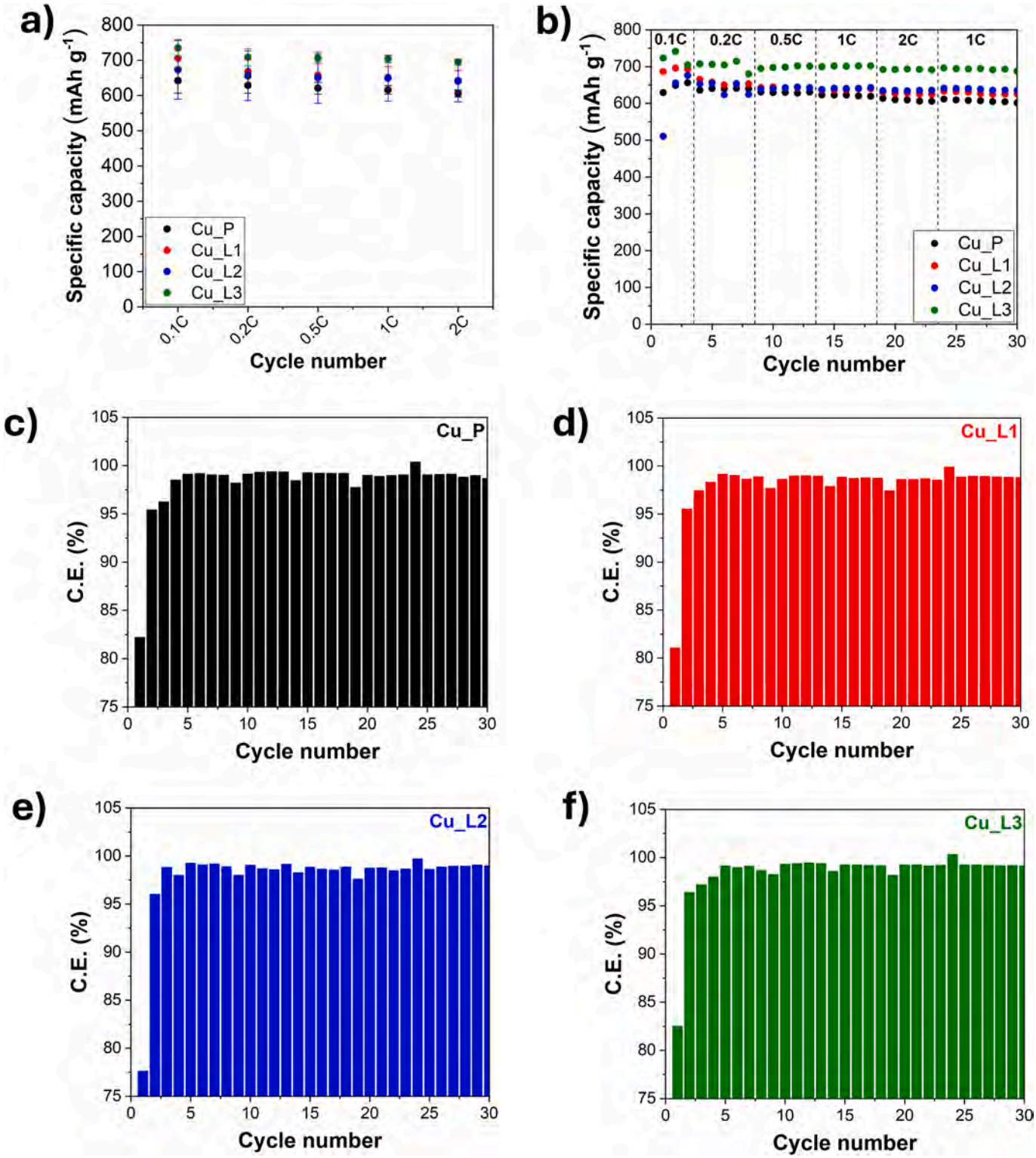


Fig. 5. Comparison of average rate capability as a function of C-rate (a) and rate capability as a function of cycle (b) for Si/C electrodes obtained using different laser treated CCs. The reported data refer to the charge capacity values of the samples. Coulombic efficiency for Si/C electrodes obtained using different laser treated CCs: Cu_P (c), Cu_L1 (d), Cu_L2 (e), Cu_L3 (f).

below 85 % for all samples (Fig. 5(c-f), Table 3), indicating that treatment of the current collector did not directly affect the cell formation process. It should be noted that the I.C.E. is typically low for silicon-based anode materials as it is closely linked to the partially irreversible process of initial silicon lithiation and formation of the SEI layer [57]. The Coulombic Efficiency (C.E.) increased up to 95 % for all samples in the second cycle, reaching an almost constant value of 99 % during subsequent cycles (Fig. 5 (c, d, e, f). Even in this case, the electrode with Cu_L3 CC demonstrated a higher Coulombic Efficiency (C.E.) compared to the Cu_L1 and Cu_L2 electrodes.

After rate capability tests, cells were charged and discharged at a constant C-rate of 1C up to 100 cycles to evaluate and compare capacity

retention over longer cycling. Fig. 6 presents capacity values for each electrode, averaged over three cycling tests. All laser treatments resulted in higher capacity retention, with Cu_L1, Cu_L2 and Cu_L3 achieving 86.9 %, 83.0 % and 84.6 %, respectively, compared to 80 % for Cu_P.

Cu_P displayed high variability at low C-rates, which decreased at higher C-rates (Fig. 6(a)). However, during charging/discharging at 1C, Cu_P exhibited a progressive increase in variability. Cu_L1 instead exhibited significant but constant variability throughout the entire charge/discharge process, both during rate capacity and capacity retention tests (Fig. 6(b)). In contrast, Cu_L2 was characterized by high variability during the entire charge/discharge process (Fig. 6(c)). Cu_L3 exhibited lowest variability of all samples both during rate capability and capacity retention tests (Fig. 6(d)). The greater fluctuation observed in the cycling results for the sample with the Cu_L2 collector can be attributed to the lower homogeneity of the collector surface produced with μ-grooves. This can be correlated to the micrographs reported in Fig. 1(c-d), referring to the Cu_L2 collector, and surface topography analyses that indicated approximately twice the increase in surface area of that achieved with Cu_L1 and Cu_L3. On the contrary, the results confirm that laser texturing of the CC via DLIP affected both rate capability and long cycle testing at constant C-rate, exhibiting better electrochemical performance than the other samples, confirming that physical modification of the CC surface helps to limit capacity loss.

The most representative replica of each CC sample was selected for a more in-depth analysis of cycling results. Fig. 7 reports detailed galvanostatic charge/discharge curves of the formation cycles and corresponding dQ/dV profiles for all tested samples. dQ/dV curves allowed a deeper examination of the specific lithiation and de-lithiation processes taking place within the silicon-based active material. The first discharge curves (black curves in Fig. 7(a), (c), (e) and (g)) and corresponding dQ/dV profiles (dashed black lines in Fig. 7(b), (d), (f) and (h)), confirmed the results observed during cyclic voltammetry analysis (Fig. 4(a)). As reported in the literature [58], all samples underwent a prominent lithiation process during the first cycle characterized by a typical plateau below 0.1 V related to the Li—Si alloying mechanism discussed previously. As a result, the charge/discharge profile and corresponding dQ/dV profile of the first lithiation cycles differed from those of subsequent cycles for all samples. During the first lithiation cycle, the material underwent a two-phase reaction between the Li-rich surface and Li-poor core due to Si—Si bond-breaking [51,59]. More specifically, the long plateau below 0.1 V observed for all the samples was due to a phase change of Li—Si alloy from a crystalline to an amorphous phase [47].

As a result of the evident difference between the first lithiation and subsequent cycles, the I.C.E. of the first cycle was below 85 % for all samples (Table 4). During the first lithiation cycle, highly stable lithiated compounds, or strong bonds, are formed between lithium atoms and site defects, especially at interfaces and grain boundaries where a high number of silicon particle defects are expected [60]. Additionally, during the first cycle, formation of the SEI layer occurs on the anode. The combination of these phenomena results in a significant loss of lithium during the first cycle.

During the de-lithiation process, all samples exhibited a similar profile characterized by four de-lithiation steps corresponding to four visible and reversible peaks in the dQ/dV profiles. These peaks were

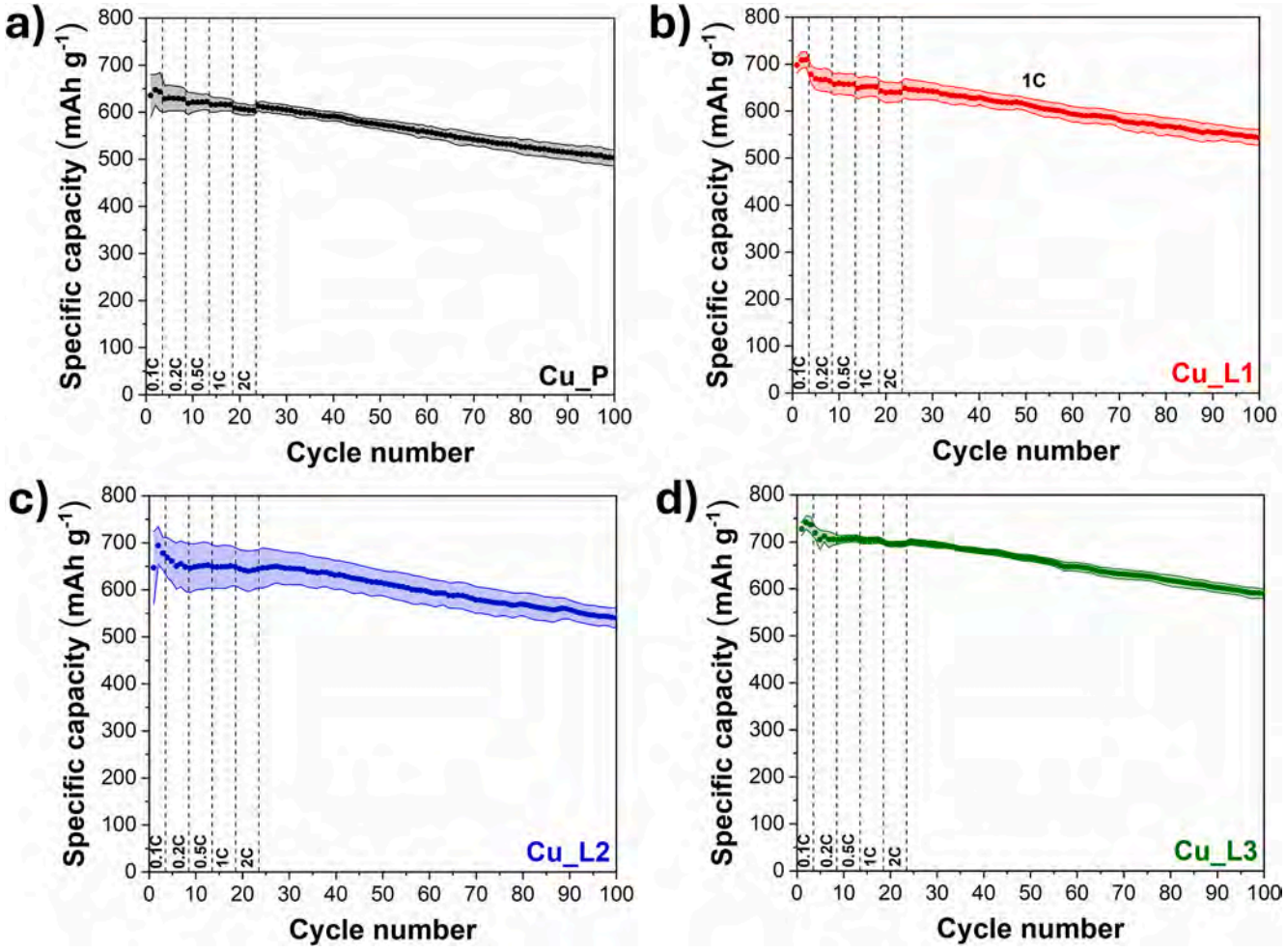


Fig. 6. Capacity retention of electrodes with different CCs. Specific capacity, averaged over three cells, for Si/C electrodes obtained with different laser textured CCs: Cu_P (a), Cu_L1 (b), Cu_L2 (c) and Cu_L3 (d).

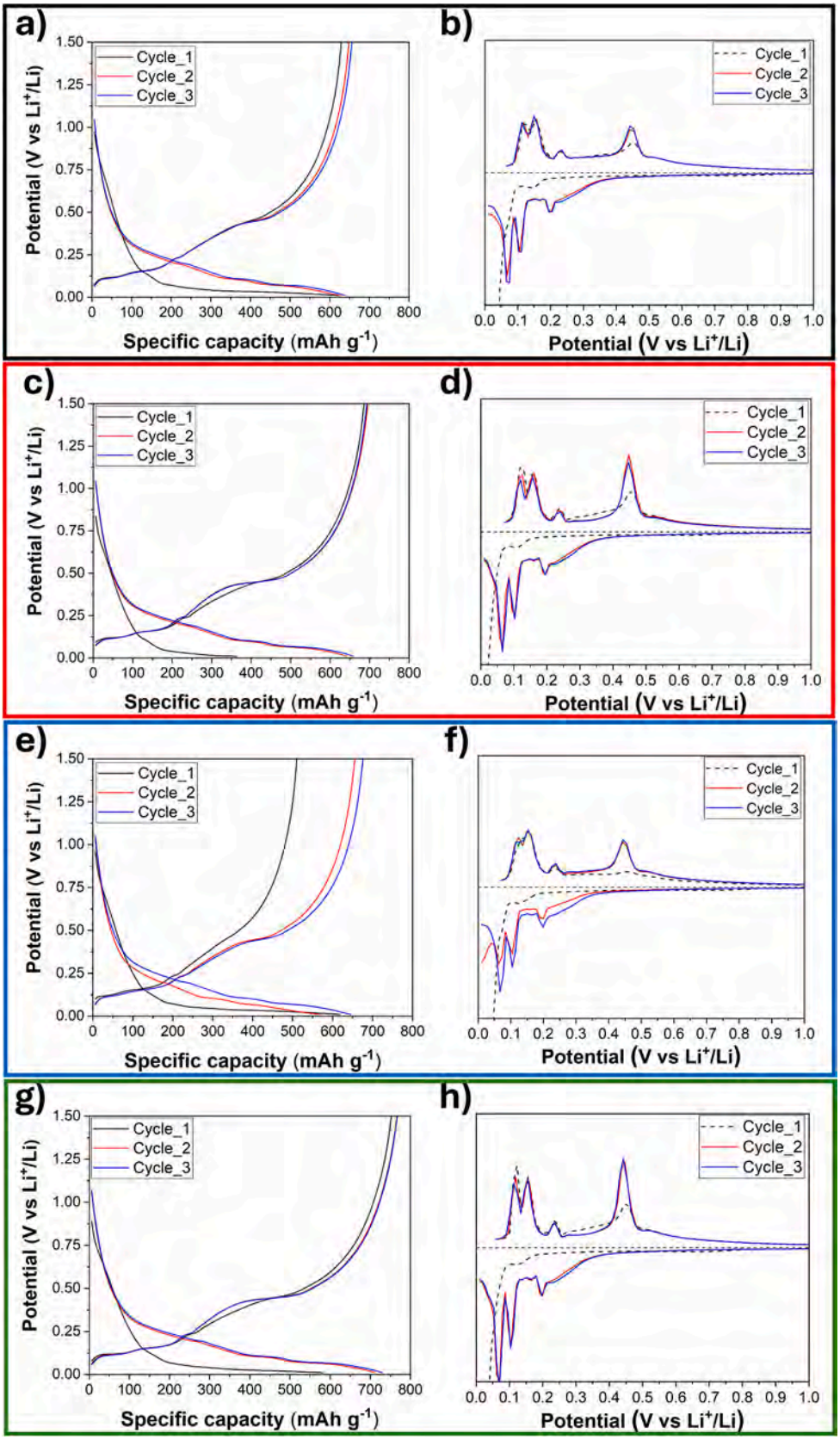


Fig. 7. Charge/discharge curves and related dQ/dV profiles for Si/C electrodes obtained using different laser-treated CCs: Cu_P (a, b), Cu_L1 (c, d), Cu_L2 (e, f) and Cu_L3 (g, h).

Table 4
Values of specific capacity, coulombic efficiency and capacity retention, averaged over three cells.

Sample name	*Cycle number*	*C-rate*	*Specific capacity (mAh g^{-1})*	*Coulombic efficiency (%)*	*Capacity retention (%)*
Cu_P	1	0.1C	635.184	82.1859	Forming
	2		647.404	95.412	
	3		642.917	96.2452	
	8	0.2C	627.791	99.0129	97.6
	13	0.5C	621.973	99.3385	96.7
	18	1C	615.633	99.1868	95.7
	23	2C	603.737	99.0261	93.9
Cu_L1	1	0.1C	697.702	81.0481	Forming
	2		708.843	95.5148	
	3		709.371	97.426	
	8	0.2C	663.873	98.8842	93.6
	13	0.5C	656.535	98.9569	92.5
	18	1C	651.441	98.7298	91.8
	23	2C	639.963	98.5307	90.2
Cu_L2	1	0.1C	592.764	76.4847	Forming
	2		655.161	95.3733	
	3		655.494	98.5394	
	8	0.2C	609.492	98.594	93.0
	13	0.5C	625.275	98.9941	95.4
	18	1C	626.383	98.8307	95.5
	23	2C	617.262	98.4952	94.2
Cu_L3	1	0.1C	727.219	82.4881	Forming
	2		741.866	96.3945	
	3		735.735	97.1893	
	8	0.2C	706.216	98.6629	96.0
	13	0.5C	707.278	99.3839	96.1
	18	1C	704.579	99.1553	95.8
	23	2C	694.052	99.2125	94.3

more pronounced for Cu_L1 and Cu_L3 samples, confirming the higher specific capacity of these electrodes during the formation cycles. In contrast, electrodes with the pristine collector (Cu_P), as well as Cu_L2, exhibited less intense and defined profiles. Notably, the Cu_L2 sample exhibited greater polarization between the lithiation profiles of the second and third cycles, as highlighted by the corresponding dQ/dV profiles.

The results of electrochemical characterization in terms of specific capacity, capacity retention and C.E., including their reproducibility, suggest that laser texturing can improve cell performance compared to untreated current collectors. In particular, LIPSS (Cu_L1) and DLIP (Cu_L3) led to measurable improvements in performance. Conversely, CCs with μ-grooves (Cu_L2) were found to achieve poor reproducibility and worse electrochemical results, indicating that attention must be paid to the appropriate selection of the laser setup and process parameters during cell optimization.

After cycling, the cells were disassembled in a glove box and the cathodes investigated by SEM to evaluate the electrode morphology after repeated charge/discharge cycles. The most significant outcome of SEM analysis was direct observation of differences in morphology between new and post-mortem samples, with a particular focus on the impact of cycling on the characteristics of the interface between the current collector and active layer of electrodes. Fig. 8 presents SEM images of electrode sections before and after cycling for the four tested electrodes. Three different magnifications were acquired in each case to allow examination of the interface morphology on different scales.

Pristine electrodes that were not subject to laser treatment exhibited irregular morphology at the interface (Cu_P, Fig. 8(a)), with minor variations in thickness and topography resulting from the original manufacturing process of the CC. In contrast, post-cycled samples exhibited clear modification of the interface between the current collector and active layer, indicating deformation of the CC due to expansion and contraction during charge/discharge cycling. Battery grade aluminum and copper employed for CCs are ductile materials, implying that plastic deformation had taken place as a result of mechanical stresses at and near the interface with the active material. Electrodes with LIPSS exhibited clear evidence of the texture generated by the laser, with regular ridges and valleys having a period of approximately 850 nm (Cu_L1, Fig. 8(b)), consistent with the outcomes of AFM analysis. Plastic deformation due to charge/discharge cycling could also be observed in this case for post-cycled samples, similar to that observed for pristine samples but with a more regular period for the smallest features, maintaining some characteristics of the original LIPSS. For electrodes with μ-grooves, the effect of laser texturing on the current collector was again evident, with a set of ridges and valleys with a period of approximately 3–4 μm (Cu_L2, Fig. 8(c)). Plastic deformation of the CC due to charge/discharge cycling was much less evident in post-cycled samples in this case compared to the other samples, with the interface geometry of new and post-mortem samples remaining relatively similar. For electrodes subject to DLIP, the effect of laser texturing could again be seen on new samples (Cu_L3, Fig. 8(d)), with ridges and valleys with a period of approximately 2.8 μm, corresponding to the base dimensions of cones observed during AFM analysis. Similarly to electrodes with LIPSS, plastic deformation of the CC due to charge and discharge cycling could be observed for post-mortem samples, but with a regular period for the smallest features, maintaining some characteristics of the original laser-textured morphology.

Among all of the tested samples, pristine electrodes exhibited greater plastic deformation than those with laser-textured CCs. Above all, however, laser texturing led to more regular deformation, appearing to control material flow during expansion and contraction of the active material during charge and discharge cycling. While plastic deformation appeared to be only slightly lower for Cu_L1 (LIPSS) and Cu_L3 (DLIP) compared to pristine samples, deformation was less evident for Cu_L2 (μ-grooves). To more fully understand the correlation between deformation and cyclability, as well as the mechanisms leading to the observed outcomes, further analysis of stresses near and at the interface during expansion of the active material must now be carried out. The outcomes of SEM analysis, however, provide direct evidence of changes in deformation during cycling as a result of laser-textured CCs. This, in turn, implies changes in mechanical stresses experienced at the interface between CCs and active materials due to laser texturing of CCs in light of the direct link between mechanical deformation and stress state.

4. Conclusion

This study highlighted the effectiveness of ultrashort pulsed laser texturing in enhancing the electrochemical performance and stability of silicon-based anodes for lithium-ion batteries. The techniques employed, achieving laser-induced periodic surface structures (LIPSS) and μ-grooves by self-remodeling phenomena, and cones via direct laser interference patterning (DLIP), significantly increased the interfacial surface area, contributing to improve the adhesion between the current collector and active material.

Electrochemical analyses revealed improved specific capacity and capacity retention for the treated CCs, if compared to untreated copper. Among the investigated sample, the DLIP-textured current collector (Cu_L3) exhibited the best performance in terms of cycling stability and reproducibility with an average specific capacity of 734.9 mAh g^{-1} during forming cycles at 0.1C and a capacity retention of 84.6 % after 100 cycles at 1C compared to 641.8 mAh g^{-1} and 80 % for pristine CCs.

Post-cycling SEM analyses confirmed that laser texturing reduced plastic deformation and evenly better distributed mechanical stresses generated during charge/discharge cycles. This suggests improved control over the volumetric expansion and contraction of the active material, contributing to higher interface stability.

The results underline the potential of ultrashort pulsed laser technology as a sustainable approach to enhance the performance and cyclability of next-generation silicon-based anode electrodes for application in LIBs. Based on these outcomes, effort must now be placed into predicting and quantifying this effect to allow more effective

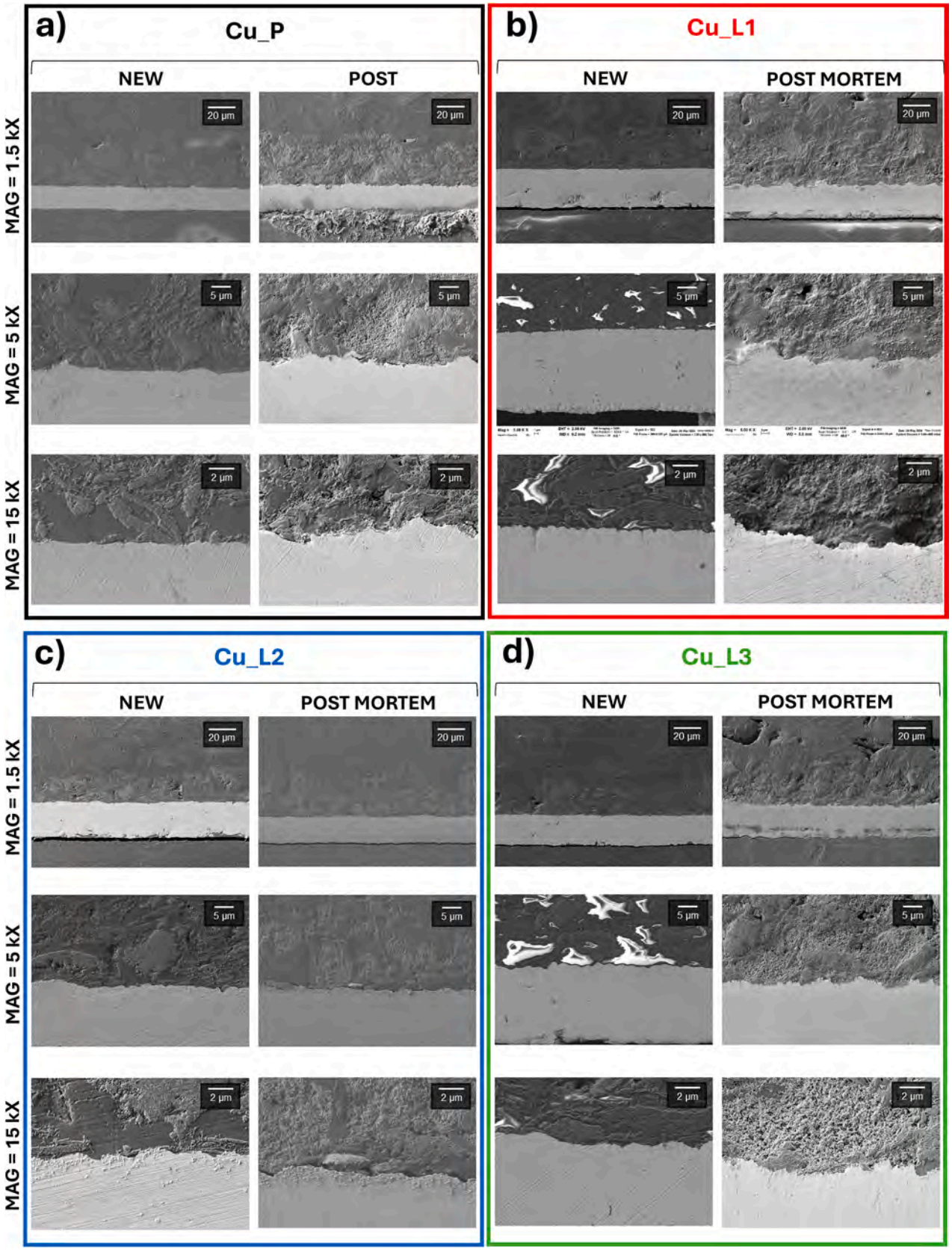


Fig. 8. SEM images of pre- and post-cycled electrode sections with various CC surface preparations: Cu_P (a), Cu_L1 (b), Cu_L2 (c), Cu_L3 (d).

optimization of laser parameters for texturing of next-generation Li-ion batteries.

CRediT authorship contribution statement

Elisa Ravesio: Writing – original draft, Methodology, Investigation, Data curation. **Giorgio Montinaro:** Writing – original draft, Methodology, Investigation, Data curation. **Girolamo Mincuzzi:** Writing – original draft, Supervision, Resources, Methodology, Funding acquisition, Data curation, Conceptualization. **Marco Negozio:** Writing – original draft, Methodology, Investigation, Data curation. **Daniele Versaci:** Writing – original draft, Visualization, Validation, Supervision, Methodology, Data curation, Conceptualization. **Valentin Gartiser:** Methodology, Investigation, Data curation. **Adrian H.A. Lutey:** Writing – original draft, Supervision, Methodology, Data curation, Conceptualization. **Federico Bella:** Writing – review & editing, Resources, Funding acquisition. **Silvia Bodoardo:** Writing – review & editing, Supervision, Resources, Funding acquisition, Conceptualization.

Declaration of competing interest

The authors declare that they have no known competing financial interests or personal relationships that could have appeared to influence the work reported in this paper.

Acknowledgements

The authors kindly acknowledge financial support received from the GIGAGREEN project (Horizon Europe, grant agreement N° 101069707).

The authors would like to thank of Dr. Francesca Rossi and Dr. Giovanna Trevisi of the IMEM-CRN Institute, Parma, for performing SEM analysis of sectioned electrodes.

The authors would like to thank CICenergiGUNE for use of the 46-point probe system (RM2610, HIOKI Corp., Japan) for measurement of the resistance of the electrodes.

Daniele Versaci acknowledges support from FSE REACT-EU - PON Ricerca e Innovazione 2014–2020 program (Ministerial Decree no. 1062/2021).

Elisa Ravesio acknowledges support from the project PNRR-NGEU which has received funding from the MUR – DM 352/2022.

Appendix A. Supplementary data

Supplementary data to this article can be found online at https://doi.org/10.1016/j.est.2024.115226.

Data availability

Data will be made available on request.

References

[1] J.T. Frith, M.J. Lacey, U. Ulissi, A non-academic perspective on the future of lithium-based batteries, Nat. Commun. 14 (2023) 420, https://doi.org/10.1038/s41467-023-35933-2.

[2] S. Dühnen, J. Betz, M. Kolek, R. Schmuch, M. Winter, T.S. Placke Dühnen, J. Betz, M. Kolek, R. Schmuch, M. Winter, T. Placke, Toward green battery cells: perspective on materials and technologies, Small Methods 4 (2020) 2000039, https://doi.org/10.1002/SMTD.202000039.

[3] M. Fichtner, K. Edström, E. Ayerbe, M. Berecibar, A. Bhowmik, I.E. Castelli, S. Clark, R. Dominko, M. Erakca, A.A. Franco, A. Grimaud, B. Horstmann, A. Latz, H. Lorrmann, M. Meeus, R. Narayan, F. Pammer, J. Ruhland, H. Stein, T. Vegge, M. Weil, Rechargeable batteries of the future—the state of the art from a BATTERY 2030+ perspective, Adv. Energy Mater. 12 (2022), https://doi.org/10.1002/aenm.202102904.

[4] H. Jeong, J. Jang, C. Jo, A review on current collector coating methods for next-generation batteries, Chem. Eng. J. 446 (2022) 136860, https://doi.org/10.1016/J.CEJ.2022.136860.

[5] P. Zhu, D. Gastol, J. Marshall, R. Sommerville, V. Goodship, E. Kendrick, A review of current collectors for lithium-ion batteries, J. Power Sources 485 (2021) 229321, https://doi.org/10.1016/J.JPOWSOUR.2020.229321.

[6] D. Versaci, R. Colombo, G. Montinaro, M. Buga, N. Cortes Felix, G. Evans, F. Bella, J. Amici, C. Francia, S. Bodoardo, Tailoring cathode materials: a comprehensive study on LNMO/LFP blending for next generation lithium-ion batteries, J. Power Sources 613 (2024) 234955, https://doi.org/10.1016/j.jpowsour.2024.234955.

[7] C. Heubner, K. Voigt, P. Marcinkowski, S. Reuber, K. Nikolowski, M. Schneider, M. Partsch, A. Michaelis, From active materials to battery cells: a straightforward tool to determine performance metrics and support developments at an application-relevant level, Adv. Energy Mater. 11 (2021) 2102647, https://doi.org/10.1002/AENM.202102647.

[8] P. Li, H. Kim, S.T. Myung, Y.K. Sun, Diverting exploration of silicon anode into practical way: a review focused on silicon-graphite composite for lithium ion batteries, Energy Storage Mater 35 (2021) 550–576, https://doi.org/10.1016/J.ENSM.2020.11.028.

[9] M. Yamada, T. Watanabe, T. Gunji, J. Wu, F. Matsumoto, Review of the design of current collectors for improving the battery performance in lithium-ion and post-lithium-ion batteries, Electrochem 1 (2020) 124–159, https://doi.org/10.3390/ELECTROCHEM1020011.

[10] M.J. Lain, J. Brandon, E. Kendrick, Design strategies for high power vs. High energy lithium ion cells, Batteries 5 (2019), https://doi.org/10.3390/batteries5040064.

[11] J.-F. Li, Y.-S. Lin, C.-H. Lin, al, B. Koo, J. Yi, C. Burm, L. Guo, D.B. Thornton, M. A. Koronfel, I.E.L. Stephens, M.P. Ryan, Degradation in lithium ion battery current collectors, J. Phys: Energy 3 (2021) 032015, https://doi.org/10.1088/2515-7655/AC0C04.

[12] Y. Yang, W. Yuan, X. Zhang, Y. Ke, Z. Qiu, J. Luo, Y. Tang, C. Wang, Y. Yuan, Y. Huang, A review on structuralized current collectors for high-performance lithium-ion battery anodes, Appl. Energy 276 (2020) 115464, https://doi.org/10.1016/J.APENERGY.2020.115464.

[13] C. Lamiel, I. Hussain, X. Ma, K. Zhang, Properties, functions, and challenges: current collectors, Mater. Today Chem. 26 (2022) 101152, https://doi.org/10.1016/j.mtchem.2022.101152.

[14] L. Guo, D.B. Thornton, M.A. Koronfel, I.E.L. Stephens, M.P. Ryan, Degradation in lithium ion battery current collectors, J. Phys: Energy 3 (2021) 032015, https://doi.org/10.1088/2515-7655/AC0C04.

[15] S. Jin, Y. Jiang, H. Ji, Y. Yu, Advanced 3D current collectors for lithium-based batteries, Adv. Mater. 30 (2018) 1802014, https://doi.org/10.1002/ADMA.201802014.

[16] H. Zheng, L. Tan, G. Liu, X. Song, V.S. Battaglia, Calendering effects on the physical and electrochemical properties of Li[Ni1/3Mn1/3Co1/3]O2 cathode, J. Power Sources 208 (2012) 52–57, https://doi.org/10.1016/J.JPOWSOUR.2012.02.001.

[17] D. Schreiner, M. Oguntke, T. Günther, G. Reinhart, Modelling of the calendering process of NMC-622 cathodes in battery production analyzing machine/material–process–structure correlations, Energ. Technol. 7 (2019) 1900840, https://doi.org/10.1002/ENTE.201900840.

[18] M. Onsrud, A.O. Tezel, S. Fotedar, A.M. Svensson, Novel carbon coating on aluminum current collectors for lithium-ion batteries, SN Appl Sci 4 (2022) 1–7, https://doi.org/10.1007/S42452-022-05103-Y/FIGURES/4.

[19] R. Wang, W. Li, L. Liu, Y. Qian, F. Liu, M. Chen, Y. Guo, L. Liu, Carbon black/graphene-modified aluminum foil cathode current collectors for lithium ion batteries with enhanced electrochemical performances, J. Electroanal. Chem. 833 (2019) 63–69, https://doi.org/10.1016/J.JELECHEM.2018.11.007.

[20] S. Yoon, H.S. Jang, S. Kim, J. Kim, K.Y. Cho, Crater-like architectural aluminum current collectors with superior electrochemical performance for Li-ion batteries, J. Electroanal. Chem. 797 (2017) 37–41, https://doi.org/10.1016/J.JELECHEM.2017.05.017.

[21] S. Pedaballi, C.C. Li, Effects of surface modification and organic binder type on cell performance of water-processed Ni-rich Li(Ni0.8Co0.1Mn0.1)O2 cathodes, J. Power Sources 472 (2020) 228552, https://doi.org/10.1016/J.JPOWSOUR.2020.228552.

[22] W. Pfleging, Recent progress in laser texturing of battery materials: a review of tuning electrochemical performances, related material development, and prospects for large-scale manufacturing, International Journal of Extreme Manufacturing 3 (2020) 012002, https://doi.org/10.1088/2631-7990/ABCA84.

[23] W. Pfleging, A review of laser electrode processing for development and manufacturing of lithium-ion batteries, Nanophotonics 7 (2018) 549–573, https://doi.org/10.1515/NANOPH-2017-0044/ASSET/GRAPHIC/J_NANOPH-2017-0044_FIG_014.JPG.

[24] F.L.E. Usseglio-Viretta, W. Mai, A.M. Colclasure, M. Doeff, E. Yi, K. Smith, Enabling fast charging of lithium-ion batteries through secondary- /dual- pore network: part I - analytical diffusion model, Electrochim. Acta 342 (2020) 136034, https://doi.org/10.1016/J.ELECTACTA.2020.136034.

[25] A. Sikora, L. Gemini, M. Faucon, G. Mincuzzi, Benefits of femtosecond laser 40 MHz burst mode for Li-ion battery electrode structuring, Materials 17 (2024) 881, https://doi.org/10.3390/MA17040881.

[26] L. Romoli, A.H.A. Lutey, G. Lazzini, Laser texturing of Li-ion battery electrode current collectors for improved active layer interface adhesion, CIRP Ann. 71 (2022) 481–484, https://doi.org/10.1016/J.CIRP.2022.04.034.

[27] E. Ravesio, A.H.A. Lutey, D. Versaci, L. Romoli, S. Bodoardo, Nanosecond pulsed laser texturing of Li-ion battery electrode current collectors: electrochemical characterisation of cathode half-cells, Sustain. Mater. Technol. 38 (2023) e00751, https://doi.org/10.1016/J.SUSMAT.2023.E00751.

[28] A. Sikora, M. Faucon, L. Gemini, R. Kling, G. Mincuzzi, LIPSS and DLIP: from hierarchical to mutually interacting, homogeneous, structuring, Appl. Surf. Sci. 591 (2022) 153230, https://doi.org/10.1016/J.APSUSC.2022.153230.
[29] F. Fraggelakis, G. Mincuzzi, J. Lopez, I. Manek-Hönninger, R. Kling, Controlling 2D laser nano structuring over large area with double femtosecond pulses, Appl. Surf. Sci. 470 (2019) 677–686, https://doi.org/10.1016/J.APSUSC.2018.11.106.
[30] G. Mincuzzi, L. Gemini, M. Faucon, R. Kling, Extending ultra-short pulse laser texturing over large area, Appl. Surf. Sci. 386 (2016) 65–71, https://doi.org/10.1016/J.APSUSC.2016.05.172.
[31] S. Alamri, F. Fraggelakis, T. Kunze, B. Krupop, G. Mincuzzi, R. Kling, A.F. Lasagni, On the interplay of DLIP and LIPSS upon ultra-short laser pulse irradiation, Materials 12 (2019) 1018, https://doi.org/10.3390/MA12071018.
[32] P. Tallone, S. Spriano, D. Versaci, S. Ferraris, A. Tori, S. Bodoardo, Picosecond laser texturing of Al current collector to improve cycling performances and simplify recycling of Lithium-ion batteries, Surfaces and Interfaces 51 (2024) 104659, https://doi.org/10.1016/j.surfin.2024.104659.
[33] Y. Wang, Z. Zhao, J. Zhong, T. Wang, L. Wang, H. Xu, J. Cao, J. Li, G. Zhang, H. Fei, J. Zhu, Hierarchically micro/nanostructured current collectors induced by ultrafast femtosecond laser strategy for high-performance lithium-ion batteries, Energy Environ. Mater. 5 (2022) 969–976, https://doi.org/10.1002/EEM2.12223.
[34] G. Mincuzzi, L. Vesce, M. Schulz-Ruhtenberg, E. Gehlen, A. Reale, A. Di Carlo, T. M. Brown, Taking temperature processing out of dye-sensitized solar cell fabrication: fully laser-manufactured devices, Adv. Energy Mater. 4 (2014) 1400421, https://doi.org/10.1002/AENM.201400421.
[35] M. Gutierrez, M. Morcrette, L. Monconduit, Y. Oudart, P. Lemaire, C. Davoisne, N. Louvain, R. Janot, Towards a better understanding of the degradation mechanisms of Li-ion full cells using Si/C composites as anode, J. Power Sources 533 (2022) 231408, https://doi.org/10.1016/j.jpowsour.2022.231408.
[36] F. Fraggelakis, J. Lopez, I. Manek-Hönninger, G. Mincuzzi, R. Kling, Texturing metal surface with MHz ultra-short laser pulses, Opt. Express 25 (15) (2017) 18131–18139, https://doi.org/10.1364/OE.25.018131.
[37] G.D. Tsibidis, C. Fotakis, E. Stratakis, From ripples to spikes: a hydrodynamical mechanism to interpret femtosecond laser-induced self-assembled structures, Phys Rev B Condens Matter Mater Phys 92 (2015) 041405, https://doi.org/10.1103/PHYSREVB.92.041405/FIGURES/4/MEDIUM.
[38] G. Mincuzzi, A. Bourtereau, L. Gemini, S. Parareda, S. Rzepa, M. Koukolíková, P. Konopík, R. Kling, Through the forming process of femtosecond-laser nanotextured sheets for production of complex 3D parts, Appl. Sci. 13 (2023) 12500, https://doi.org/10.3390/APP132212500.
[39] C.V. Ngo, D.M. Chun, Control of laser-ablated aluminum surface wettability to superhydrophobic or superhydrophilic through simple heat treatment or water boiling post-processing, Appl. Surf. Sci. 435 (2018) 974–982, https://doi.org/10.1016/J.APSUSC.2017.11.185.
[40] D. Lou, T. Li, E. Liang, B. Lin, W.-X. He, L.-W. Jiang, Y. Lai, J. Huang, J. Guo, Z. Yang, J. Zhao, Effect of nanosecond laser treatment parameters on surface wettability behaviour of pure aluminium, IOP Conf Ser Mater Sci Eng 538 (2019) 012021, https://doi.org/10.1088/1757-899X/538/1/012021.
[41] J. Li, C. Daniel, D. Wood, Materials processing for lithium-ion batteries, J. Power Sources 196 (2011) 2452–2460, https://doi.org/10.1016/J.JPOWSOUR.2010.11.001.
[42] H. Oh, G.-S. Kim, B.U. Hwang, J. Bang, J. Kim, K.-M. Jeong, Development of a feasible and scalable manufacturing method for PTFE-based solvent-free lithium-ion battery electrodes, Chem. Eng. J. 491 (2024) 151957, https://doi.org/10.1016/j.cej.2024.151957.
[43] N. Kumano, Y. Yamaguchi, Y. Akimoto, A. Ohshima, H. Nakamura, M. Yamamura, Migration of binder and conductive agent during drying process of Li-ion battery cathodes, J. Power Sources 591 (2024) 233883, https://doi.org/10.1016/j.jpowsour.2023.233883.
[44] E.-C. Cho, C.-W. Chang-Jian, Y.-J. Wu, S.-H. Chao, J.-H. Huang, K.-C. Lee, H. C. Weng, S.-C. Hsu, Modification of aluminum current collectors with laser-scribed graphene for enhancing the performance of lithium ion batteries, J. Power Sources 506 (2021) 230060, https://doi.org/10.1016/j.jpowsour.2021.230060.
[45] M.J. Lain, G. Apachitei, D.-E. Dogaru, W.D. Widanage, J. Marco, M. Copley, Measurement of anisotropic volumetric resistivity in lithium ion electrodes, RSC Adv. 13 (2023) 33437–33445, https://doi.org/10.1039/D3RA06412C.
[46] A.L. Michan, M. Leskes, C.P. Grey, Voltage dependent solid electrolyte interphase formation in silicon electrodes: monitoring the formation of organic decomposition products, Chem. Mater. 28 (2016) 385–398, https://doi.org/10.1021/acs.chemmater.5b04408.
[47] W.J. Legerstee, T. Noort, T.K. van Vliet, H. Schut, E.M. Kelder, Characterisation of defects in porous silicon as an anode material using positron annihilation Doppler Broadening Spectroscopy, Applied Nanoscience (Switzerland) 12 (2022) 3399–3408, https://doi.org/10.1007/s13204-022-02550-2.
[48] Y. Liu, X. Liu, Y. Zhu, J. Wang, W. Ji, X. Liu, Scalable synthesis of pitch-coated nanoporous Si/graphite composite anodes for lithium-ion batteries, Energy Fuel 37 (2023) 4624–4631, https://doi.org/10.1021/acs.energyfuels.2c03702.
[49] S. Yin, Q. Ji, X. Zuo, S. Xie, K. Fang, Y. Xia, J. Li, B. Qiu, M. Wang, J. Ban, X. Wang, Y. Zhang, Y. Xiao, L. Zheng, S. Liang, Z. Liu, C. Wang, Y.-J. Cheng, Silicon lithium-ion battery anode with enhanced performance: multiple effects of silver nanoparticles, J. Mater. Sci. Technol. 34 (2018) 1902–1911, https://doi.org/10.1016/j.jmst.2018.02.004.
[50] A. Mukanova, A. Nurpeissova, S. Kim, M. Myronov, Z. Bakenov, N-type doped silicon thin film on a porous Cu current collector as the negative electrode for Li-ion batteries, ChemistryOpen 7 (2018) 92–96, https://doi.org/10.1002/open.201700162.
[51] J. Kim, M.H. Kim, Y. Kim, M.S. Kim, A. Choi, K.M. Jeong, H.W. Lee, Unveiling the role of electrode-level heterogeneity alleviated in a silicon-graphite electrode under operando microscopy, Energy Storage Mater 57 (2023) 269–276, https://doi.org/10.1016/J.ENSM.2023.02.025.
[52] Z. Yan, S. Yi, X. Li, J. Jiang, D. Yang, N. Du, A scalable silicon/graphite anode with high silicon content for high-energy lithium-ion batteries, Mater Today Energy 31 (2023) 101225, https://doi.org/10.1016/J.MTENER.2022.101225.
[53] Q. Xu, Q. Wang, D. Chen, Y. Zhong, Z. Wu, Y. Song, G. Wang, Y. Liu, B. Zhong, X. Guo, Silicon/graphite composite anode with constrained swelling and a stable solid electrolyte interphase enabled by spent graphite, Green Chem. 23 (2021) 4531–4539, https://doi.org/10.1039/d1gc00630d.
[54] Y. Xu, G. Yin, Y. Ma, P. Zuo, X. Cheng, Nanosized core/shell silicon@carbon anode material for lithium ion batteries with polyvinylidene fluoride as carbon source, J. Mater. Chem. 20 (2010) 3216–3220, https://doi.org/10.1039/b921979j.
[55] M. Ashuri, Q. He, Y. Liu, L.L. Shaw, Investigation towards scalable processing of silicon/graphite nanocomposite anodes with good cycle stability and specific capacity, Nano Mater. Sci. 2 (2020) 297–308, https://doi.org/10.1016/j.nanoms.2019.11.004.
[56] T. Jiang, S. Zhang, X. Qiu, W. Zhu, L. Chen, Preparation and characterization of silicon-based three-dimensional cellular anode for lithium ion battery, Electrochem. Commun. 9 (2007) 930–934, https://doi.org/10.1016/j.elecom.2006.11.031.
[57] L. Sun, Y. Liu, J. Wu, R. Shao, R. Jiang, Z. Tie, Z. Jin, A review on recent advances for boosting initial coulombic efficiency of silicon anodic lithium ion batteries, Small 18 (2022), https://doi.org/10.1002/smll.202102894.
[58] Z. Yuan Feng, W. Jie Peng, Z. Xing Wang, H. Jun Guo, X. Hai Li, G. Chun Yan, J. Xi Wang, Review of silicon-based alloys for lithium-ion battery anodes, Int. J. Miner. Metall. Mater. 28 (2021) 1549–1564, https://doi.org/10.1007/s12613-021-2335-x.
[59] M.J. Loveridge, M.J. Lain, I.D. Johnson, A. Roberts, S.D. Beattie, R. Dashwood, J. A. Darr, R. Bhagat, Towards high capacity Li-ion batteries based on silicon-graphene composite anodes and sub-micron V-doped LiFePO4 cathodes, Sci. Rep. 6 (1) (2016) 1–11, https://doi.org/10.1038/srep37787.
[60] T. Jia, G. Zhong, Y. Lv, N. Li, Y. Liu, X. Yu, J. Zou, Z. Chen, L. Peng, F. Kang, Y. Cao, Prelithiation strategies for silicon-based anode in high energy density lithium-ion battery, Green Energy & Environment 8 (2023) 1325–1340, https://doi.org/10.1016/J.GEE.2022.08.005.